


Optoelectronic Manipulation, Trapping, Splitting, and Merging of Water Droplets and Aqueous Biodroplets Based on the Bulk Photovoltaic Effect

Andrés Puerto,¹ Angel Méndez,² Luis Arizmendi,^{1,3} Angel García-Cabañes¹ and Mercedes Carrascosa^{1,3,*}

¹*Departamento de Física de Materiales, Facultad de Ciencias, Universidad Autónoma de Madrid, Calle Francisco Tomás y Valiente 7, E-28049 Madrid, Spain*

²*Departamento de Mecánica de Fluidos y Propulsión Aeroespacial, ETSIAE, Universidad Politécnica de Madrid, Plaza Cardenal Cisneros 3, E-28040 Madrid, Spain*

³*Instituto Nicolás Cabrera, Universidad Autónoma de Madrid, E-28049 Madrid, Spain*

 (Received 3 February 2020; revised 19 May 2020; accepted 13 July 2020; published 17 August 2020)

Optical and optoelectronic techniques for micro- and nano-object manipulation are becoming essential tools in nano- and biotechnology. The use of photovoltaic optoelectronic tweezers is a remarkable optoelectronic technique that has undergone rapid development in recent years, with excellent results and widespread potential applications. It is based on light-induced electric fields generated by the bulk photovoltaic effect in certain ferroelectrics, such as LiNbO_3 . The technique is simple and versatile, enabling the successful manipulation of a large variety of micro- and nano-objects with only optical control, without the need for electrodes or power supplies. However, the handling of objects in aqueous solutions remains a challenge for this tool, due to the electric-screening effects of polar liquids. This has hindered their application in biotechnology and biomedicine, where most processes occur in aqueous solution. Here, an efficient route to overcome this problem is proposed and demonstrated. It uses photovoltaic optoelectronic tweezers to manipulate aqueous droplets, immersed in a nonpolar oil liquid, but hanging at the air-oil interface. In this singular configuration, the high electric fields generated by the bulk photovoltaic effect in the LiNbO_3 substrate allow simple and flexible manipulation of aqueous droplets controlled by the light. Droplet guiding, trapping, merging, and splitting are achieved and efficient operation with water and a variety of biodroplets (DNA, sperm, and phosphate-buffered saline solutions) is demonstrated. A discussion on the physical mechanisms responsible for the manipulation processes is also provided. The reported results overcome the main limitation of these tweezers to handle biomaterials and promise high potential for biotechnological and biochemistry applications, including their implementation in optofluidic devices.

DOI: [10.1103/PhysRevApplied.14.024046](https://doi.org/10.1103/PhysRevApplied.14.024046)

I. INTRODUCTION

Optical manipulation has become a key tool for nano- and biotechnology. The two main optical techniques involve the use of optical [1,2] and optoelectronic tweezers [3,4]. Optical tweezers are very efficient in the manipulation of single dielectric particles, such as silica or polystyrene beads [5,6], but they use high intensities that can damage biosystems [7,8]. In turn, optoelectronic tweezers use a photoconductor substrate under an ac electric field and operate at lower intensities, providing larger forces and are better adapted for massive particle manipulation. However, they need electrodes and power supplies that complicate the devices. In both approaches, the trapping effects disappear when the light is turned off, preventing their use for the fabrication of stable traps or patterns.

Recently, an optoelectronic approach that uses a patterned photoconductive coating to overcome this latter problem has been proposed, providing remarkable results, although substrate fabrication is considerably more complicated [9].

In the last decade, another optoelectronic technique, the use of so-called photovoltaic optoelectronic tweezers (PVOT), has been introduced [10–13]. They are simpler because they operate at low light intensity without electrodes or power supplies. Recently, PVOT have experienced a remarkable development, succeeding in the manipulation, trapping, and patterning of a large variety of micro- and nano-objects, including particles (metal, dielectric, organic, etc.; see Refs. [14,15] and references therein) and nonpolar liquid (oil) droplets [16–18]. They are based on the bulk photovoltaic effect, which allows the light-induced generation of very high electric field patterns (100–200 kV/cm) inside certain ferroelectrics, such as $\text{LiNbO}_3\text{:Fe}$ [19]. These photoinduced electric fields

*m.carrascosa@uam.es

extend outside the active optical material and are able to manipulate micro- and nano-objects, mainly through dielectrophoretic forces [14,20].

This technique is very efficient for massive manipulation and patterning of nano-objects immersed in a non-polar fluid, such as air, tetradecane, or hexane [12,14]. Moreover, different from other optical and optoelectronic techniques, the photovoltaic (PV) field remains after illumination ceases, giving stability to the patterns. The PVOT technique also shows excellent reconfiguration capabilities [21,22]. These properties allow efficient fabrication of a variety of nanoparticle patterns for different applications, such as photonic devices [23] or plasmonic platforms [24]. However, PVOT have serious difficulties in handling objects inside polar liquids, such as aqueous solutions, due to electric-field-screening effects, greatly limiting potential applications in biophotonics and biotechnology. Even so, a few interesting applications have already been reported, involving cells [25,26], bacteria [27], and pollen and spore grains [28]. Therefore, a route to extend the remarkable capabilities of these optoelectronic tweezers in aqueous solutions would be a key advance for biotechnological functionalities and would widen the range of applications of this powerful technique.

The strategy proposed here consists of manipulating droplets of water and bioaqueous solutions inside a non-polar immiscible oil. Since recent trends in microfluidics use droplets to miniaturize devices (droplet or digital microfluidics), our proposal opens the door to the application of this strategy in this vast and very active field [29,30] and, in particular, to its application for lab-on-a-chip devices, which are overwhelmingly used in biotechnology [31–34]. In fact, an important issue for these technologies is the development of efficient methods to manipulate droplets inside inactive-passive fluid media. Among diverse approaches [35], optoelectronic methods, such as the one proposed here, are considered an efficient alternative.

Here, we propose and investigate the use of PVOT for manipulating water and aqueous biodroplets inside a non-polar liquid medium. There has been only one previous study attempting to handle water droplets in air [16], which could be considered a nonpolar fluid. However, these experiments fail, unless the substrate is covered with a hydrophobic coating [36] because droplets in contact with the substrate increase their wettability and become immobile. In the present approach, this problem is overcome because, during manipulation, the droplets have no contact with the substrate. Two configurations of the optoelectronic substrate, parallel and perpendicular configurations [14], are tested. Experiments of droplet guiding, splitting, and trapping, either at the interface or on the substrate are reported. Moreover, merging of two different droplets is also achieved. The experiments are developed for deionized water and aqueous biodroplets containing DNA and

sperm solutions. A discussion on the physics of the manipulation process and on the possibilities of the technique is also included.

II. PHYSICAL BASIS OF PVOT

The physical basis of PVOT has been reviewed in several recent papers [13–15]. Here, we summarize the main physical concepts affecting their operation. PVOT are based on the bulk photovoltaic effect (BPE) presented by certain ferroelectric crystals (mainly lithium niobate doped with iron [14], but also with copper [37] impurities). LiNbO₃ is a material with trigonal symmetry, highly ferroelectric, and with relevant optical properties of great interest for many photonic applications [38]. When doped with iron, it presents a very high BPE [19]. The iron impurities appear in two valence states, Fe²⁺ and Fe³⁺, which act as electron donors and acceptors, respectively, as outlined in Fig. 1(a). The BPE arises from asymmetric photoexcitation of electrons from donor impurities (Fe²⁺) to the conduction band [see the schematics of Fig. 1(b)], due to the noncentrosymmetric crystal lattice, that gives rise to an electric PV current along the ferroelectric polar axis (also called the *c* axis, a term we use in the text). For spatially homogeneous light intensity, the photovoltaic electric current density can be written as [14]

$$j_{PV} = e\alpha_a\phi l_{PV} = esDl_{PV}\phi \quad (1)$$

where $\phi = I/h\nu$ is the photon flux, e is the electron charge, α_a is the absorption coefficient, s is the photoionization cross section, and D is the donor concentration (usually [Fe²⁺]). Finally, l_{PV} is the photovoltaic effective drift length. Photoexcited electrons are eventually trapped in acceptor impurities (usually [Fe³⁺]). This directional charge transport produces a bulk electric field, E_{PV} , parallel to the *c* axis. The time constant of the generation kinetics and the steady-state E_{PV} can be written as:

$$\tau^{-1} = \frac{\mu e}{\varepsilon\varepsilon_0}n, \quad E_{PV} = \frac{j_{PV}}{en\mu}, \quad (2)$$

where μ is the electron mobility; ε_0 is the vacuum permittivity; ε is the dielectric constant of the PV material; and n is the steady-state density of photoexcited electrons, which can be written as

$$n = \frac{s\phi D}{\gamma A}. \quad (3)$$

where A is the steady acceptor concentration ([Fe³⁺]) and γ is the recombination constant of acceptors that measures the probability per unit time of trapping one electron by

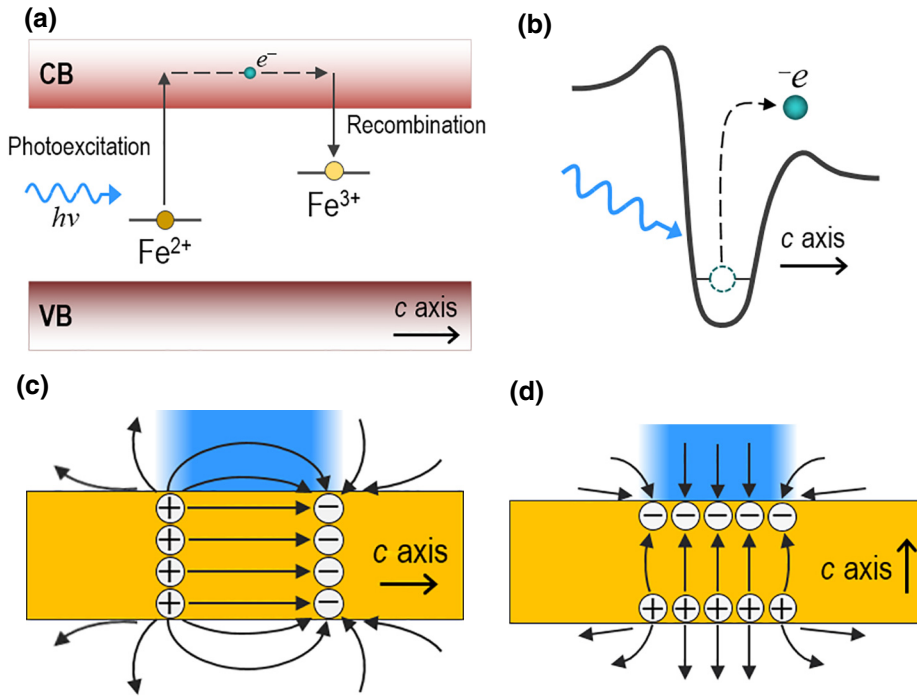


FIG. 1. (a) Schematics of the band diagram, showing the donor and acceptor levels of iron impurities and electron transport. (b) Sketch of directional photoexcitation of the valence electron of an Fe^{2+} impurity in the lithium niobate crystal. Schematics showing the PV electric field lines near the surface for (c) an x -cut crystal and (d) a z -cut crystal.

one acceptor. Using Eqs. (1) and (3), one arrives at

$$E_{\text{PV}} = \frac{I_{\text{PV}} \gamma}{\mu} A. \quad (4)$$

Then, the magnitude of the steady-state bulk photovoltaic field depends on $A = [\text{Fe}^{3+}]$, which, in turn, depends on the iron concentration $[\text{Fe}] = [\text{Fe}^{2+}] + [\text{Fe}^{3+}]$ and the oxidation state of impurities $[\text{Fe}^{3+}]/[\text{Fe}]$. Notably, the steady-state value of E_{PV} does not depend on I . The photovoltaic field persists over a long time, which depends on the dark conductivity of the sample that also depends on the doping level and oxidation state of impurities. Typical times are in the range from minutes to 1–2 years [39]. When light illumination is not homogeneous, charge transport includes an electron-diffusion term and, in general, it is described by a set of nonlinear differential equations, as established by Kukhtarev *et al.* [40].

The photovoltaic electric field extends near the surface outside the crystal, where it can act either on charged objects, via electrophoretic (EP) forces ($\mathbf{F}_{\text{EP}} = q\mathbf{E}$), or on neutral objects polarized by the field (dielectrophoretic forces), as explained in detail in previous works [20,41]. The expression for dielectrophoretic (DEP) forces on a spherical particle, particularly relevant for this work, is

$$\mathbf{F}_{\text{DEP}} = (\mathbf{p} \cdot \nabla) \mathbf{E}, \quad (5)$$

where \mathbf{p} is the dipolar momentum of the object induced by the evanescent field \mathbf{E} . Due to the crystalline and/or geometrical anisotropy of objects, the dipolar momentum

induced by the electric field obeys, in general, a tensor expression, $p_i = \alpha_{p,ij} E_j$, where $\alpha_{p,ij}$ is the polarizability tensor. Under nonoscillating electric fields (as in the case of PV fields) and for the very relevant case of spherical particles, such as the droplets investigated in this work, the polarizability becomes a scalar α_p that can be written as [20]

$$\alpha_p = 2\pi r^3 \varepsilon_m \frac{\sigma_p - \sigma_m}{\sigma_p + 2\sigma_m}, \quad (6)$$

where r is the radius of the particle or droplet; ε_m is the absolute dielectric permittivity of the host medium; and σ_m and σ_p are the conductivities of the host medium and particle, respectively. For this case, the dielectrophoretic force becomes

$$\mathbf{F}_{\text{DEP}} = \alpha_p \nabla (\mathbf{E})^2. \quad (7)$$

Regarding the photovoltaic substrates, there are two main useful geometries, the parallel (x - or y -cut crystals) and perpendicular (z -cut crystals) configurations, which have the c axis parallel or normal to the active surface, respectively [42], as illustrated in Figs. 1(c) and 1(d) for homogeneous illumination. One can see that the structure of the space-charge distribution and the corresponding evanescent electric field are different for these two geometries (see also simulations in Sec. V), and thus, they provide different manipulation schemes.

III. STRATEGY FOR AQUEOUS DROPLET MANIPULATION AND EXPERIMENTAL METHODS

As already mentioned, we propose a strategy for the PVOT manipulation of biological material. This technique consists of acting on aqueous biodroplets as highly polarizable “microparticles,” immersed in a nonpolar immiscible oil without contact with the PV substrate, and thus, avoiding direct screening of the bulk photoinduced electric fields.

Since water normally has a higher density than that of immiscible oils, a water droplet immersed inside an oil would fall onto the substrate under the action of gravity. However, in our strategy, the aqueous droplet is deposited on the surface of a suitable oil in such a way that it remains hanging at the oil-air boundary, as shown by the lateral photograph in Fig. 2(a), corresponding to a real experiment. This droplet configuration is studied in detail in Refs. [43,44]. The droplet stays at the interface due to compensation of the apparent weight, F_w' (downward force), with a net upward force, F_γ [see Fig. 2(b)], arising from the simultaneous action of the water-air, water-oil, and oil-air surface-tension forces. For a stable hanging droplet, suitable values of the surface-tension coefficients, oil density, and volume of the droplet are required. This hanging-droplet strategy is a key advantage because it prevents the droplet from sinking and depositing on the substrate, where it would be immobilized by electrowetting [45] and it would no longer be possible to move the droplet. Thus, with the proposed strategy, easy and flexible optical manipulation of water droplets is expected.

Specifically, as a nonpolar immiscible liquid, we use paraffin oil with a dielectric constant of $\varepsilon = 4.6\text{--}4.8$,

density of $\rho \approx 0.876\text{ g/cm}^3$, and viscosity of $\eta = 0.230\text{ Pa s}$ (at 20°C). The layer of paraffin oil has a thickness, h , over the crystal ranging between 1 and 2 mm. The volume of the droplets ranges between 0.05 and $1\ \mu\text{l}$. As PV substrates, we use 1-mm-thick z -cut and x -cut plates of $\text{LiNbO}_3:\text{Fe}$ with an iron concentration of $2.4 \times 10^{19}\text{ cm}^{-3}$ and an estimated ratio of $[\text{Fe}^{3+}]/[\text{Fe}]$ of about 0.83.

In Fig. 2(c), a scheme of the optical system used to the PVOT is drawn. Basically, it consists of an optical microscope, where a laser beam is coupled through the objective lens, so that it can be focused on the active substrate to generate the PV electric fields. Two CMOS cameras record top and lateral views of the sample holder, respectively. This sample holder [inset in Fig. 2(c)] is a glass cuvette with optical-quality surfaces containing transparent paraffin oil. The $\text{LiNbO}_3:\text{Fe}$ active substrate is placed at the bottom of the cuvette and aqueous droplets are added with a micropipette on the surface of the paraffin layer.

The manipulation capabilities extend to droplets of a variety of aqueous liquids of interest in biophotonics technology, such as deionized water (Type II water), phosphate-buffered saline (PBS) cell culture medium, and aqueous solutions containing sperm or fluorescein-tagged fragmented DNA.

IV. EXPERIMENTAL RESULTS ON DROPLET MANIPULATION

Let us now describe a series of experiments to investigate the performance of the proposed strategy. Different kinds of processes, such as controlled droplet moving, trapping, merging, and splitting, are attempted. The illuminating laser beam has a Gaussian profile with a peak intensity I_p and a standard deviation σ_G , i.e., the light

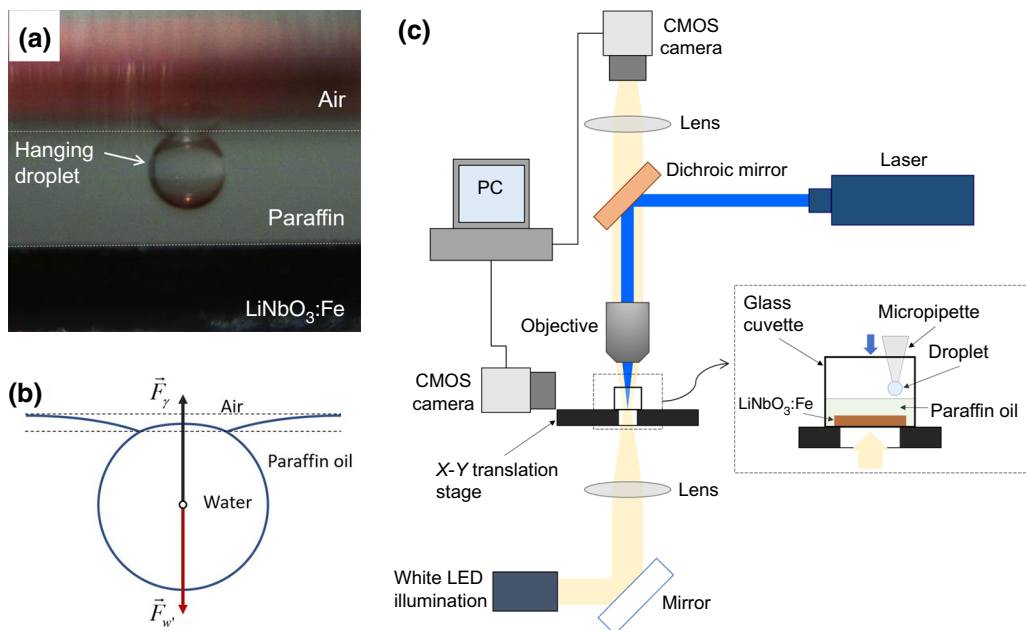


FIG. 2. (a) Photograph of the lateral view of a stable hanging water droplet used in our experiments. Boundaries between different media are indicated with discontinuous white lines. (b) Diagram of a water droplet on an oil (paraffin) surface in equilibrium, showing the forces acting downwards and upwards. (c) Schematics of the optical microscope system of the PVOT used, showing, in detail, the sample holder as an inset.

intensity profile is

$$I(r) = I_p \exp\left(-\frac{r^2}{2\sigma_G^2}\right). \quad (8)$$

For all experiments, $\sigma_G = 120 \mu\text{m}$, although I_p ranges from 5 to -500 W cm^{-2} . Here, we define the beam diameter as the distance $4\sigma_G$, for which the corresponding circle includes about 99% of the Gaussian beam power.

The two substrate geometries (z and x cut), for which the symmetry of the photoinduced electric fields is different, are tested to find the best configuration for each manipulation process.

A. Droplet moving and trapping on the PV substrate

The first set of experiments aim to move droplets from a variety of available aqueous liquids (water and DNA, sperm, and PBS aqueous solutions) and using the perpendicular configuration (z -cut crystals). A diode Gaussian laser beam ($\lambda = 488 \text{ nm}$) is focused on the substrate to a diameter of $4\sigma_G = 480 \mu\text{m}$. An illustrative experiment with a droplet of an aqueous solution of fluorescein-tagged DNA is shown in Fig. 3, where a peak light intensity of 30 W cm^{-2} is used. Initially, still in the dark, a droplet with a volume of $0.2 \mu\text{l}$ (diameter $d \approx 0.7 \text{ mm}$) is pipetted and remains hanging at the paraffin-air interface [Fig. 3(a)]. The paraffin oil layer thickness is $h = 1.1 \text{ mm}$. Then, the laser beam is focused on the substrate at a horizontal distance of 2.5 mm from the droplet. When the laser light is switched on, the droplet starts to move, and it approaches the illumination region due to the evanescent electric field components generated by the $\text{LiNbO}_3:\text{Fe}$ substrate [Figs. 3(b) and 3(c)] that induce DEP forces on the droplet (see Sec. V). When the droplet arrives at the illuminated region, it is elongated in the vertical direction due to the vertical component of the evanescent electric field [Figs. 3(d) and 3(e)] and it makes contact with the substrate at a point close to but shifted ($\sim 500 \mu\text{m}$) from the

center of the light spot. Then, the droplet wets the crystal surface and becomes trapped on it [Figs. 3(f)–3(h)]. The inset of Fig. 3(h) shows a magnified fluorescence image of the trapped droplet. Moreover, the monitoring of the entire process can be seen in Video 1 within the Supplemental Material [46]. Once droplets are trapped on the substrate, they can no longer be displaced by moving the light beam. This is in accordance with data reported in Ref. [36], where only by covering the substrate with a hydrophobic layer can the water droplet be moved.

In this experiment, illumination and manipulation are carried out simultaneously, but the manipulation process can also be made after illumination because, as mentioned, the PV fields remain in the dark. This latter “sequential” procedure has been mostly used in previously reported works for particle patterning [14] and is also attempted here for all kinds of aqueous droplets. The droplets are deposited at the air-paraffin interface after the substrate is illuminated for 1 min. The droplet moves in the dark to the previously illuminated region and is finally trapped on the substrate, adjacent to the light beam (again shifted $\sim 500 \mu\text{m}$ from the center), following a process similar to that of Fig. 3. These shifts are discussed in Sec. V. The process is shown in Fig. 4 for a deionized water droplet.

B. Droplet trapping at the interface and merging of two droplets

In previous experiments, the attractive vertical component of the DEP force is high enough to produce droplet trapping on the substrate. However, for certain purposes, it can be advantageous to immobilize the droplet at the interface without it falling on the PV substrate. To this end, we use larger thicknesses, h , of the paraffin oil layer. This avoids contact between the elongated droplet and the substrate, keeping the droplet hanging at the oil-air interface. Notably, a larger h also decreases the vertical DEP force component acting on the droplet, and thus, reduces its vertical elongation. The experiments are performed

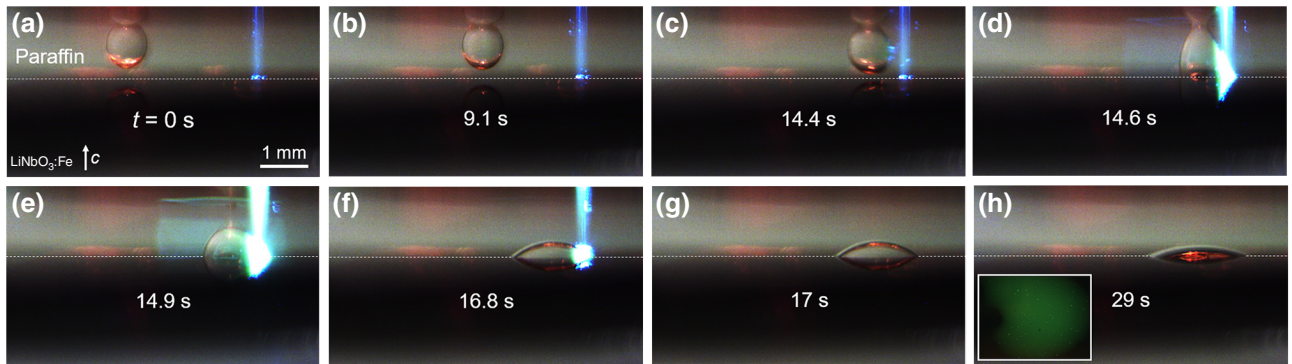


FIG. 3. Photographs taken by the CMOS lateral camera of droplet manipulation (a)–(d) and trapping (e)–(h) on the z -cut substrate. Solution contains fluorescein-tagged DNA. (Droplet volume $V = 0.2 \mu\text{l}$ and laser beam intensity $I_p = 30 \text{ W cm}^{-2}$.) Inset in (h) shows a top-view image of the trapped droplet taken with a fluorescence microscope. Timescale is indicated at the top of each image.

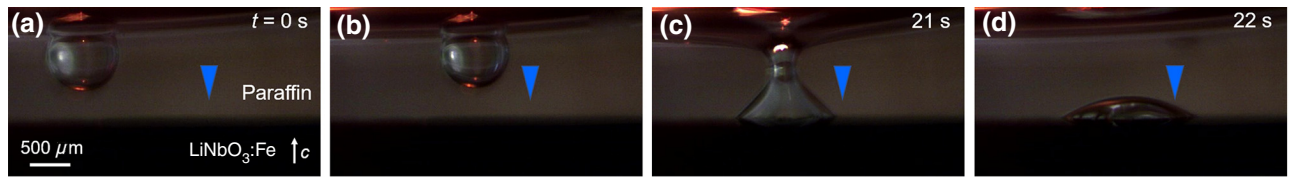


FIG. 4. Photographs taken by the CMOS lateral camera for a deionized water droplet moving after illumination. Position of the previous illumination is indicated by a blue arrow. (a) Addition of the droplet, (b) droplet movement, and (c),(d) trapping on the crystal. ($V = 0.2 \mu\text{l}$ and $I_p = 300 \text{ W cm}^{-2}$.) Timescale is indicated at the top of each image. Paraffin layer thickness $h = 0.85 \text{ mm}$. Initial distance from the droplet to the light spot is 1.5 mm .

with water and aqueous biodroplets. After traveling toward the light spot, the hanging droplet is fixed close to, but again slightly shifted from, the center of the light beam at the paraffin-air interface. An illustrative experiment with $I_p = 8 \text{ W cm}^{-2}$ and $h = 1.25 \text{ mm}$ is shown in Fig. 5, where three images of droplet motion approaching the light beam (from bottom to top) are presented, together with a curve showing the time evolution of the droplet position. The droplet diameter is 0.6 mm and the initial position of the droplet is 1.6 mm from the center of the light spot. This curve clearly shows how the droplet starts to move; accelerates up to a velocity of about $65 \mu\text{m/s}$; and, finally, stops and stays fixed very close to the light beam shifted about $150 \mu\text{m}$ from its center. The process can be also observed in Video 2 within the Supplemental Material [46].

In summary, PVOT allow two kinds of droplet trapping, either at the paraffin-air interface or on the substrate.

In addition, this capability enables another kind of manipulation process with high potential for a variety of

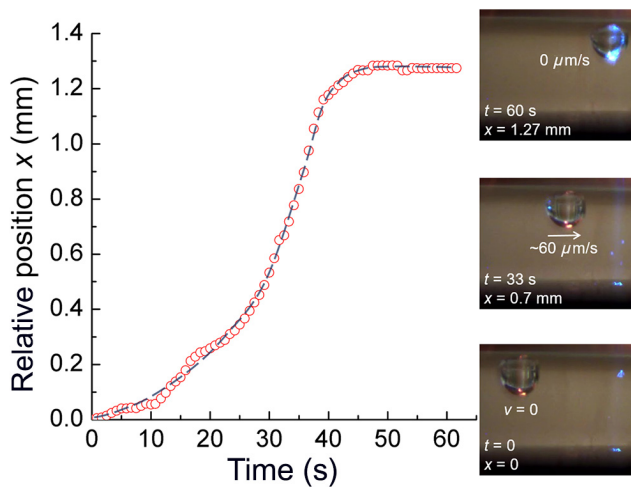


FIG. 5. Time evolution of the water droplet position when moving under the action of PVOT using a z -cut LiNbO_3 substrate. Right: three insets with photographs corresponding to three different moments of the time evolution. Droplet position, velocity, and time are indicated in each image. Laser peak intensity of $I_p = 8 \text{ W cm}^{-2}$, droplet volume of $V = 0.1 \mu\text{l}$, and $h = 1.25 \text{ mm}$.

applications in optofluidics: the merging of two aqueous droplets. The merging experiment obviously requires the deposition of two droplets at the interface, and it is conducted as follows (see Fig. 6 and Video 3 within the Supplemental Material [46]). One of the droplets is immobilized by illuminating it, while the second droplet starts to move towards the light beam [Figs. 6(a)–6(e)], and finally the two droplets merge when they come into contact [Fig. 6(f)].

C. Droplet splitting

Finally, the last kind of experiments aim to split droplets. To this end, we use the parallel configuration (x -cut crystal) whose symmetry seems more appropriate because it has a preferential direction (c -axis) on the active surface. Splitting is expected along this direction. In fact, although it is also attempted with the isotropic perpendicular configuration (z -cut crystals), no splitting results are obtained.

To achieve droplet splitting, the substrate is illuminated ($I_p = 130 \text{ W cm}^{-2}$), attracting one droplet to the beam spot, as shown in Figs. 7(a)–7(c) through top-view photographs. Next, by adjusting the beam on the droplet center, it is immobilized [Figs. 7(d) and 7(e)]. Then, the droplet starts to elongate along the c axis [Figs. 7(f) and 7(g)], and, for suitable parameters (in this case, light spot diameter of $4\sigma_G = 480 \mu\text{m}$, droplet diameter of $d = 500 \mu\text{m}$, and paraffin layer thickness of $h = 1 \text{ mm}$), it split into two parts of similar volume [Fig. 6(h)]. The complete process is shown in Video 4 within the Supplemental Material [46].

It is worthwhile noting that, in this experiment, the droplet is moved and immobilized at the interface [Figs. 7(a)–7(c)] before splitting, demonstrating that these processes are also possible in the parallel configuration of the substrate. In addition, merging is also obtained for this parallel substrate geometry, although the perpendicular configuration can be considered as preferable because efficient operation seems to require a lower light intensity.

V. DISCUSSION ON PHYSICAL MECHANISMS

The reported experiments provide a solid proof of concept for the proposed strategy to handle aqueous droplets

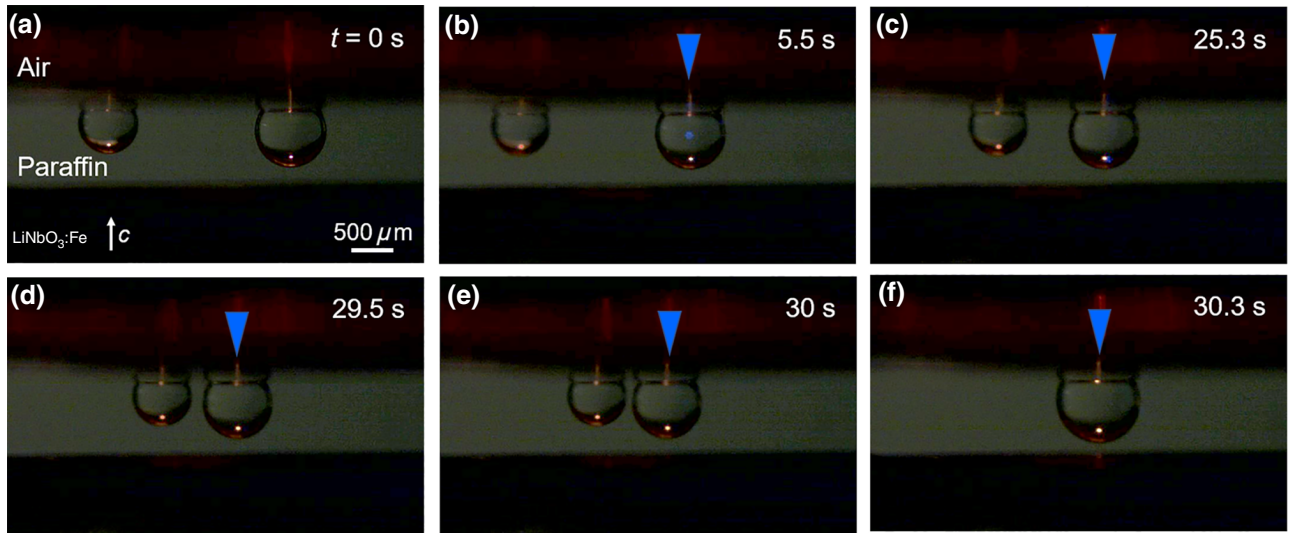


FIG. 6. Photographs taken by the lateral CMOS camera of the merging process using a z -cut substrate. Position of the laser beam (not visible) is marked by a blue arrow. (a) Initial situation. (b) Turning on the laser beam on one droplet. (c)–(e) Shift of the left droplet towards the light beam, and thus, towards the other droplet. (f) Larger hanging droplet resulting from the merging of the two former ones. Initial droplet volumes are $0.2 \mu\text{l}$ and $0.4 \mu\text{l}$. Laser beam intensity is 8 W cm^{-2} and paraffin layer thickness is 1 mm .

by PVOT. Let us now analyze the physical mechanisms involved. To this end, calculations of the PV electric fields and the corresponding DEP force and potential under Gaussian-beam illumination are conducted. As already mentioned in Sec. II, when the photovoltaic substrate is illuminated with a nonhomogeneous light beam, such as a Gaussian beam, a rigorous theoretical description requires solving a set of nonlinear differential equations, the Kukhtarev's equations [40,47]:

$$\frac{\partial n}{\partial t} = s\phi D - \gamma n A - \frac{1}{e} \nabla \cdot \mathbf{j}, \quad (9)$$

$$\frac{\partial D}{\partial t} = -\frac{\partial A}{\partial t} = -s\phi D + \gamma n A, \quad (10)$$

$$\mathbf{j} = e\mu n \mathbf{E} - eD_c \nabla n + es\phi D l_{pv} \mathbf{u}_{pv}, \quad (11)$$

and the generated electric field is calculated by Gauss's law:

$$\nabla(\epsilon_0 \epsilon \mathbf{E}) = e(n + D - D_0), \quad (12)$$

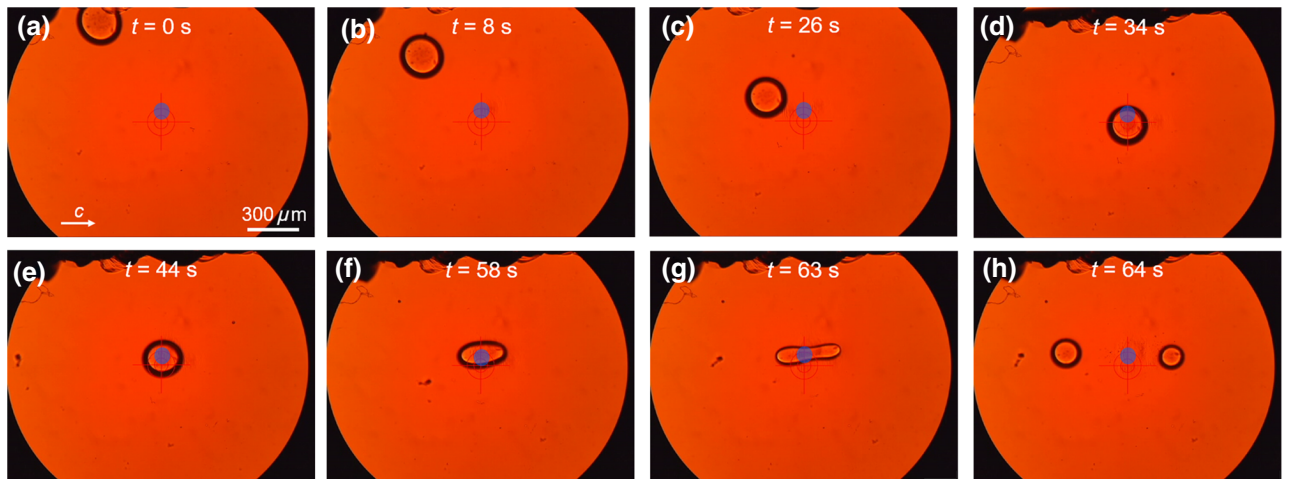


FIG. 7. Sequence of top-view photographs, showing a water droplet moving toward the light beam (the center of which is indicated by a blue dot) (a)–(d) and splitting into two droplets (e)–(h), using an x -cut $\text{LiNbO}_3:\text{Fe}$ crystal. Timescale is indicated at the top of each image. Droplet volume is $0.05 \mu\text{l}$ and laser beam intensity is 130 W cm^{-2} .

TABLE I. Material parameters of $\text{LiNbO}_3\text{:Fe}$ used in the numerical calculations.

Parameter	Magnitude
ε (paraffin)	4.6
ε_{33} (LiNbO_3)	29.1
$[\text{Fe}^{2+}]$	$4 \times 10^{24} \text{ m}^{-3}$
$[\text{Fe}^{2+}]$	$2 \times 10^{25} \text{ m}^{-3}$
μ	$-5 \times 10^{-6} \text{ m}^2 \text{ V}^{-1} \text{ s}^{-1}$
γ	$10^{-15} \text{ m}^3 \text{ s}^{-1}$
s	$2 \times 10^{-22} \text{ m}^2$
l_{PV}	$5 \times 10^{-10} \text{ m}$

where D_c is the diffusion coefficient, \mathbf{u}_{PV} is the unit vector along the c -axis direction, and D_0 is the initial donor concentration. Other parameters are already defined in Sec. II. These equations are solved by numerical calculations, with the COMSOL Multiphysics software and using the parameter values indicated in Sec. III and in Table I. More details on the theoretical model and calculations can be found in several previous papers from our group [41,48] and particularly in Ref. [49].

To gain a first insight into the physics of the PVOT, we calculate the space-charge distribution and the electric fields generated by the photovoltaic effect under Gaussian-beam illumination, such as that of the experiments with $\sigma_G = 120 \mu\text{m}$ and $I_p = 8 \text{ W cm}^{-2}$. The results are shown in Fig. 8 for an illumination time of $t = 30 \text{ s}$ and for the two crystal configurations, z cut [Figs. 8(a)–8(c)] and x cut [Figs. 8(d)–8(f)]. Schematics for the two geometries are depicted in Figs. 8(a) and 8(d), respectively, indicating the direction of the c axis, and the two planes, parallel and normal to the active surface, for which the results of

the calculations are shown. In turn, Figs. 8(b) and 8(c) (z cut) and Figs. 8(e) and 8(f) (x cut) show the simulations for the electric field vectors (arrows with lengths plotted on a logarithmic scale) and the space-charge density generated by the photovoltaic current (using a color code). On one hand, in the z -cut scheme, the photovoltaic current [see Eq. (1)] generates negative surface charge at the $+c$ face [Figs. 8(b) and 8(c) in red color] and positive surface charge at the opposite $-c$ face (not shown in Fig. 8). On the other hand, in the x -cut scheme, the redistribution of charge is parallel to the active surface and a dipolar charge distribution appears along the c axis [Figs. 8(e) and 8(f)]. Looking at planes parallel to the active surface [Figs. 8(c) and 8(f)], one can distinguish different symmetries of the electric field lines, isotropic for the z -cut system [Fig. 8(c)], and exhibiting an axial symmetry about the c axis for the x -cut system [Fig. 8(f)]. Different charges and electric field structures of the two crystal cuts are responsible for the differences in the manipulation capabilities (mainly regarding droplet splitting) found for the two substrate configurations.

Once we analyze the photovoltaic effect in the substrate responsible for the operation of PVOT, let us focus our discussion on the specific experimental results of moving, trapping, and merging using the perpendicular configuration (z cut) described in Secs. IV A and IV B. Aqueous droplets are expected to be globally neutral, and thus, in the presence of PV electric fields, droplets should experience dielectrophoretic forces, F_{DEP} [described by Eqs. (5)–(7)]. In fact, most previous results with PVOT acting on solid particles can also be explained by the action of these DEP forces [14,15]. Then, we calculate these forces and the corresponding dielectrophoretic potentials from the

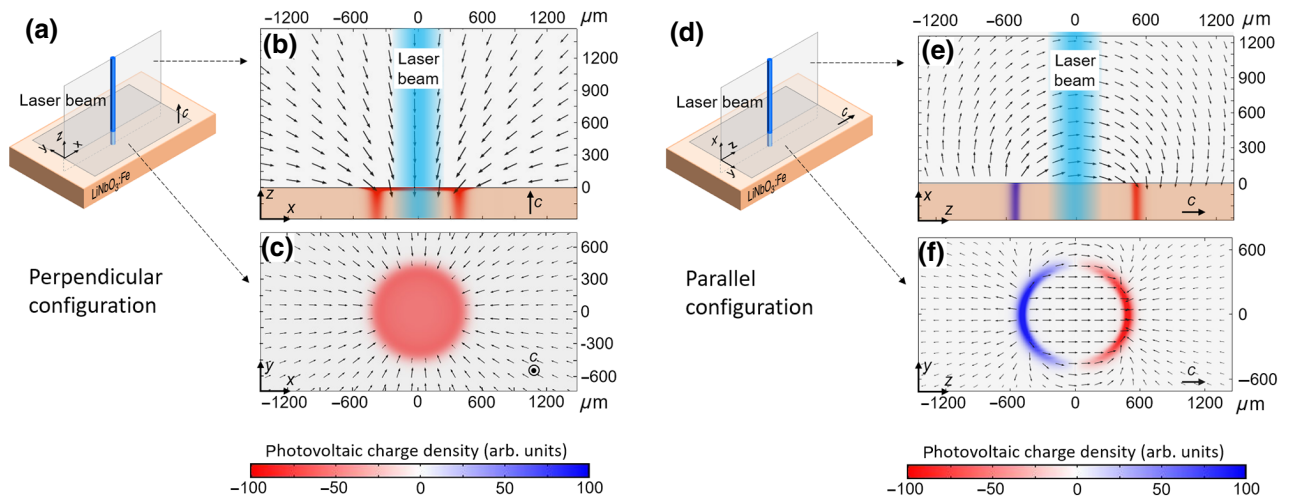


FIG. 8. Spatial distribution of the PV field (arrows) outside the crystal and space-charge density (color map) for the perpendicular (a)–(c) and parallel (d)–(f) configurations, along two planes as indicated in the insets. Parallel planes correspond to a vertical distance of $10 \mu\text{m}$ from the substrate, i.e., very close to it. Blue laser beam is drawn in (a), (b), (d), and (e). Lengths of arrows, in arbitrary units, are plotted using a logarithmic scale.

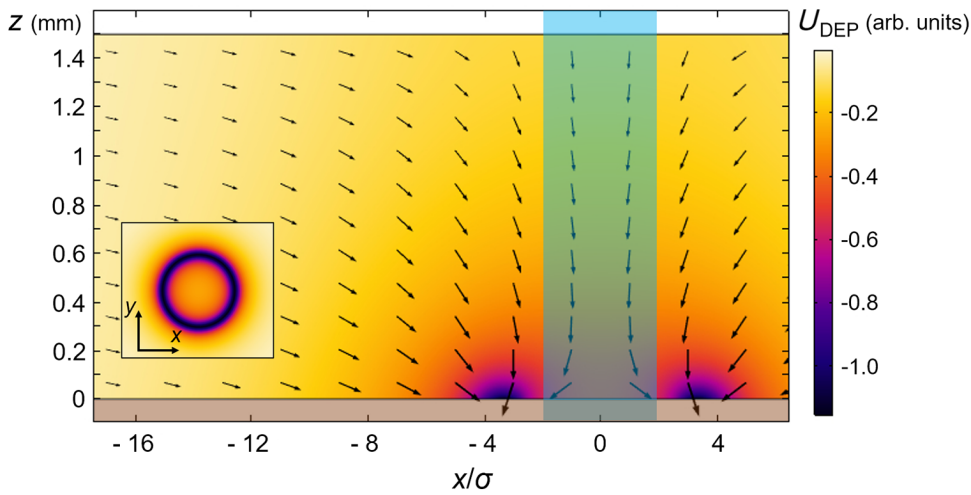


FIG. 9. Color map of the simulated dielectrophoretic potential in z -cut crystal under Gaussian-beam illumination. Arrows represent the DEP force; their lengths, in arbitrary units, are plotted using a logarithmic scale. Inset on the left shows a top view, X - Y plane at $10\ \mu\text{m}$ from the crystal surface, of the DEP potential.

photovoltaic electric fields for the same Gaussian-beam intensity as that in Fig. 8. In Fig. 9, the spatial distribution of the DEP potential for a time illumination of 30 s is shown using a color map. Moreover, the arrows (plotted using a logarithmic scale) indicate the DEP forces. Due to the z -cut crystal geometry, the DEP potential and forces, have a radial symmetry around the center of the light beam, i.e., along the X - Y plane, as seen in the inset. Notably, the potential well has a ring minimum around this center with a radius of $r \approx 4\sigma_G = 480\ \mu\text{m}$. When the droplet is relatively far from the light illumination source, the DEP force has only a small horizontal component that pushes the droplet along the interface toward the illuminated region. However, as it approaches the light beam, the vertical component increases, and the droplet begins to elongate vertically to approach the substrate. If the vertical component is strong enough, the droplet comes into contact with the substrate and, assisted by the high substrate wettability, becomes trapped on it. One can expect that the droplet should be trapped at the minimum of the DEP potential. Hence, the existence of the ring absolute minimum in the potential (clearly shown in the inset of Fig. 9) explains the experimental observation of droplet trapping at a position deviated ($\sim 500\ \mu\text{m}$) from the center of the light beam, as seen in Figs. 3(d)–3(e). The explanation for this subtle experimental feature by theory supports the key role attributed to DEP forces. Notably, in the case of the electrophoretic potential, its minimum appears at the center of the beam illumination, as discussed in Ref. [41]. It is remarkable that the electric field and the DEP forces remain after illumination, and thus, manipulation can be performed in the dark (Fig. 4) under the action of the same electrical forces involved when light is present. On one hand, manipulation in the dark is another advantage for this flexible technique in some cases, e.g., to avoid any damaging effects of light on biomaterials. On the other hand, it provides further confirmation that photovoltaic electric fields are the basis of the manipulation processes.

If the vertical component of the DEP force close to the light beam is not large enough, the hanging droplet cannot come into contact with the substrate and it is immobilized at the air-paraffin interface (Fig. 5). This experiment, with a one-dimensional droplet trajectory along the interface, with no observed droplet deformation until it is rather close to the light beam, is particularly suitable for a more detailed analysis of the droplet dynamics with a simple model. Droplet motion is initiated by the horizontal component of the DEP force, $F_{\text{DEP},h}$, but, obviously, once it starts to move, a horizontal friction force, F_f , appears. Then, during motion, the net horizontal force will be $F_{T,h} = F_{\text{DEP},h} - F_f$. Additionally, F_f can be evaluated approximately by the Stokes force for spherical particles, $F_f = 6\pi R\eta v$, where R and v are the droplet radius ($R = 0.3\ \mu\text{m}$) and velocity, respectively, and η is the dynamic paraffin viscosity ($\eta = 0.230\ \text{Pa s}$).

Moreover, the time evolution of the droplet velocity and acceleration can be inferred from the experimental curve, $x(t)$, from the corresponding derivatives. Then, from the acceleration, we can obtain the experimental net force, $F_{T,h}$, and, from the velocity, we obtain the approximate friction force, F_f . The obtained $F_{T,h}$ is in the range of a few pN, whereas the friction force, as estimated by the Stokes' formula, is in the order of μN , with a maximum value of $0.1\ \mu\text{N}$. This indicates that friction compensates nearly instantaneously for the magnitude of the horizontal component of the DEP force, i.e., $F_{\text{DEP},h} = F_{T,h} + F_f \approx F_f$, so that $F_f = 6\pi R\eta v$ give us an experimental estimation of $F_{\text{DEP},h}$. These estimated values obtained from experiments compare rather well with the calculated horizontal component of the DEP force, which provides values in the same order of magnitude, although somewhat higher, to those of the experimental ones. For instance, the maximum theoretical value of $F_{\text{DEP},h}$ occurs roughly at the same distance to the beam center as that in the experiment and its value is about $0.4\ \mu\text{N}$.

The PVOT capability of trapping droplets at the interface is useful for droplet merging: when two droplets are present, both are attracted to the illuminating region by DEP forces and they can be merged, as seen in Fig. 6.

The last experiments, consisting of droplet splitting (Fig. 7), are conducted only in the parallel configuration (x -cut substrate). Splitting occurs after elongation along the c axis when the light beam is placed at the center of the droplet. This is a rather complicated process, in which droplet elongation is at the origin of the phenomenon and can be understood in terms of the structure of light-induced electric fields, as simulated in Figs. 8(e) and 8(f), for the x -cut geometry. Notably, in the x -cut substrate, the PV fields are mainly parallel to the active surface at the center of the light beam [Figs. 8(e) and 8(f)], whereas they are essentially vertical in the perpendicular configuration [Figs. 8(b) and 8(c)]. When the light beam is only at the center of the illuminated region, it polarizes the droplet parallel to the PV field, i.e., horizontally along the c axis. The positive droplet pole become close to the negatively charged substrate region and the negative droplet pole is close to the positively charged substrate region. The horizontal components of the electric field, dominant in the parallel configuration, elongate the droplet, and they can split it when its size and distance to the substrate reach suitable values. In fact, the time evolution of the light-induced charge distribution on the crystal (as seen in Video 5 within the Supplemental Material [46]) should favor the process: the distance between the positively and negatively charged substrate regions increases with time to facilitate droplet splitting. Finally, other manipulation processes, namely, moving, trapping, and merging, also observed in this parallel configuration, can be qualitatively explained by DEP forces, analogously to the case of the perpendicular geometry.

VI. SUMMARY AND OUTLOOK

A strategy to manipulate water- and biodroplets by PVOT is proposed and demonstrated, overcoming the main remaining challenge of these tweezers. Among optoelectronic methods, the technique presented here is simple and cheap. It uses a laser beam that generates active electric fields in the photovoltaic substrate (LiNbO₃:Fe) without electrodes or power supplies and without any further processing of its surface. The main active phenomenon responsible for droplet manipulation is the bulk photovoltaic effect, which is particularly high in LiNbO₃:Fe, that generates light-induced electric fields as high as 250 kV/cm in the proximity of the crystal [50]. The experiments can be explained satisfactorily in terms of the PV fields and DEP forces associated with these evanescent electric fields outside the substrate. Moreover, the experimental results on the dynamics of the droplet allow

estimates of the DEP force to be obtained that are consistent with theoretical values.

The applied strategy for droplet manipulation shows key advantages: the droplet hanging at the interface can be manipulated easily and a variety of processes, such as guiding, trapping at the interface and on the substrate, merging of two droplets, and splitting, can be realized. These functionalities stem from the peculiar behavior of the hanging droplet and the flexible manipulation capabilities presented by PVOT, including those provided by the two crystal geometries (parallel and perpendicular) and those arising by operation under illumination or after it in the dark. Therefore, the main outcome of this work is a solution for overcoming the bottleneck that exists for the flexible manipulation of water and aqueous biodroplets by PVOT, providing an efficient tool for optofluidic applications in bio and nanotechnology.

Regarding its potential use for biotechnology devices, DNA aqueous droplets, diluted sperm, and PBS (for cell culture) droplets are manipulated, and thus, applications in genetics or cell biology are envisaged. Moreover, one can expect that the manipulation capabilities also extend to any other aqueous droplets with application in diverse areas of biology, physics, or chemistry. In addition, the method is well adapted for implementation in optofluidic devices. For instance, achieving optically controlled droplet merging is a key capability for applications in chemical synthesis or biotechnological essays [29].

In fact, in some previous studies using PVOT, the action on particles immersed in nonpolar liquids has been developed inside microfluidic chips [12,51]. Furthermore, ferroelectric platforms based in lithium niobate have already been used to generate tiny droplets using the pyroelectric effect [52,53] or the photovoltaic effect [54]. Then, particularly in the latter case, one could combine, in the same optically controlled platform, droplet generation and manipulation functionalities. Further developments in these directions should provide key advances in the near future.

ACKNOWLEDGMENTS

Financial support from the Ministerio de Ciencia, Innovación y Universidades of Spain (Grant No. MAT2017-83951-R) is gratefully acknowledged. A.P. acknowledges funding under the Iniciativa de Empleo Juvenil y Fondo Social Europeo (Grant No. PEJ2018-003989). The authors also thank Dr. Carmen López-Fernández and Professor José Luis Bella (Departamento de Biología, Universidad Autónoma de Madrid) for providing the biological material.

-
- [1] A. Ashkin, Acceleration and Trapping of Particles by Radiation Pressure, *Phys. Rev. Lett.* **24**, 156 (1970).

- [2] A. Ashkin and J. M. Dziedzic, Optical levitation by radiation pressure, *Appl. Phys. Lett.* **19**, 283 (1971).
- [3] P. Y. Chiou, A. T. Ohta, and M. C. Wu, Massively parallel manipulation of single cells and microparticles using optical images, *Nature* **436**, 370 (2005).
- [4] M. C. Wu, Optoelectronic tweezers, *Nat. Photonics* **5**, 322 (2011).
- [5] A. Ashkin, J. M. Dziedzic, J. E. Bjorkholm, and S. Chu, Observation of a single-beam gradient force optical trap for dielectric particles, *Opt. Lett.* **11**, 288 (1986).
- [6] S. E. Skelton and K. Dholakia, Trapping in a material world, *ACS Photonics* **3**, 719 (2016).
- [7] A. Ashkin and J. M. Dziedzic, Optical trapping and manipulation of viruses and bacteria, *Science* **235**, 1517 (1987).
- [8] P. Rodríguez-Sevilla, L. Labrador-Páez, D. Jaque, and P. Haro-González, Optical trapping for biosensing: Materials and applications, *J. Mater. Chem.* **5**, 9085 (2017).
- [9] S. Zhang, N. Shakiba, Y. Chen, Y. Zhang, P. Tian, J. Singh, M. D. Chamberlain, M. Satkauskas, A. G. Flood, N. P. Kherani, S. Yu, P. W. Zandstra, and A. R. Wheeler, Patterned optoelectronic tweezers: A new scheme for selecting, moving, and storing dielectric particles and cells, *Small* **14**, 1803342 (2018).
- [10] H. A. Eggert, F. Y. Kuhnert, K. Buse, J. R. Adleman, and D. Psaltis, Trapping of dielectric particles with light-induced space-charge fields, *Appl. Phys. Lett.* **90**, 241909 (2007).
- [11] X. Zang, J. Wang, B. Tang, X. Tan, R. A. Rupp, L. Pan, Y. Kong, Q. Sun, and J. Xu, Optical trapping and manipulation of metallic micro/nanoparticles via photorefractive crystals, *Opt. Express* **17**, 9981 (2009).
- [12] M. Esseling, F. Holtmann, M. Woerdemann, and C. Denz, Two-dimensional dielectrophoretic particle trapping in a hybrid crystal/PDMS-system, *Opt. Express* **18**, 17404 (2010).
- [13] J. Villarroel, H. Burgos, A. García-Cabañes, M. Carrascosa, A. Blázquez-Castro, and F. Agulló-López, Photovoltaic versus optical tweezers, *Opt. Express* **19**, 24320 (2011).
- [14] M. Carrascosa, A. García-Cabañes, M. Jubera, J. B. Ramiro, and F. Agulló-López, LiNbO₃: A photovoltaic substrate for massive parallel manipulation and patterning of nano-objects, *Appl. Phys. Rev.* **2**, 040605 (2015).
- [15] A. García-Cabañes, A. Blázquez-Castro, L. Arizmendi, F. Agulló-López, and M. Carrascosa, Recent achievements on photovoltaic optoelectronic tweezers based on lithium niobate, *Crystals* **8**, 65 (2018).
- [16] L. Chen, S. Li, B. Fan, W. Yan, D. Wang, L. Shi, H. Chen, D. Ban, and S. Sun, Dielectrophoretic behaviours of microdroplet sandwiched between LN substrates, *Sci. Rep.* **6**, 29166 (2016).
- [17] L. Chen, B. Fan, W. Yan, S. Li, L. Shi, and H. Chen, Photo-assisted splitting of dielectric microdroplets in a LN-based sandwich structure, *Opt. Lett.* **41**, 4558 (2016).
- [18] F. Li, X. Zhang, K. Gao, L. Shi, Z. Zan, Z. Gao, C. Liang, E. R. Mugisha, H. Chen and W. Yan, All-optical splitting of dielectric microdroplets by using a y-cut-LN-based anti-symmetrical sandwich structure, *Opt. Express* **27**, 25767 (2019).
- [19] E. M. De Miguel, J. Limeres, M. Carrascosa, and L. Arizmendi, Study of developing thermal fixed holograms in LiNbO₃, *J. Opt. Soc. Am. B* **17**, 1440 (2000).
- [20] T. B. Jones, *Electromechanics of Particles* (Cambridge University Press, Cambridge, UK, 1995).
- [21] S. Glaesener, M. Esseling, and C. Denz, Multiplexing and switching of virtual electrodes in optoelectronic tweezers based on lithium niobate, *Opt. Lett.* **37**, 3744 (2012).
- [22] C. Sebastián-Vicente, E. Muñoz-Cortés, A. García-Cabañes, F. Agulló-López, and M. Carrascosa, Real-time operation of photovoltaic optoelectronic tweezers: New strategies for massive nano-object manipulation and reconfiguration patterning, *Part. Part. Syst. Charact.* **36**, 1900233 (2019).
- [23] J. F. Muñoz-Martínez, M. Jubera, J. Matarrubia, A. García-Cabañes, F. Agulló-López, and M. Carrascosa, Diffractive optical devices produced by light-assisted trapping of nanoparticles, *Opt. Lett.* **41**, 432 (2016).
- [24] I. Elvira, J. F. Muñoz-Martínez, M. Jubera, A. García-Cabañes, J. L. Bella, P. Haro-González, M. A. Díaz-García, F. Agulló-López, and M. Carrascosa, Plasmonic enhancement in the fluorescence of organic and biological molecules by photovoltaic tweezing assembly, *Adv. Mater. Technol.* **2**, 1700024 (2017).
- [25] A. Blázquez-Castro, J. C. Stockert, B. López-Arias, A. Juarranz, F. Agulló-López, A. García-Cabañes, and M. Carrascosa, Tumour cell death induced by bulk photovoltaic effect of LiNbO₃:Fe under visible light irradiation, *Photochem. Photobiol. Sci.* **10**, 956 (2011).
- [26] Blázquez-Castro A. García-Cabañes and M. Carrascosa, Biological application of ferroelectric materials, *appl. Phys. Rev.* **5**, 041101 (2018).
- [27] L. Miccio, V. Marchesano, M. Mugnano, S. Grilli, and P. Ferraro, Light induced DEP for immobilizing and orientation escherichia coli bacteria, *Opt. Lasers Eng.* **76**, 34 (2016).
- [28] M. Jubera, I. Elvira, A. García-Cabañes, J. L. Bella, and M. Carrascosa, Trapping and patterning of biological objects using photovoltaic tweezers, *Appl. Phys. Lett.* **108**, 023703 (2016).
- [29] S. Mashaghi, A. Abbaspourrad, D. A. Weitz, and A. M. van Oijen, Droplet microfluidics: A tool for biology, chemistry and nanotechnology, *Trends Anal. Chem.* **82**, 118 (2016).
- [30] L. Pang, J. Ding, X. X. Liu, and S. K. Fan, Digital microfluidics for cell manipulation, *Trends Anal. Chem.* **117**, 291 (2019).
- [31] Y. Bai, M. Gao, L. Wen, C. He, Y. Chen, C. Liu, X. Fu, and S. Huang, Applications of microfluidics in quantitative biology, *Biotechnol. J.* **13**, 1700170 (2018).
- [32] T. Trantidou, M. S. Friddin, A. Salehi-Reyhani, O. Ces, and Y. Elani, Droplet microfluidics for the construction of compartmentalized model membranes, *Lab Chip* **18**, 2488 (2018).
- [33] J. Schimtz, T. Noll, and A. Grünberger, Heterogeneity studies of mammalian cells for bioproduction: From tools to application, *Trends Biotechnol.* **37**, 645 (2019).
- [34] Y. Yang, Y. Chen, H. Tang, N. Zong, and X. Jiang, Microfluidics for biomedical analysis, *Small Method.* **4**, 1900451 (2020).
- [35] A. Fornell, C. Johannesson, S. S. Searle, A. Happstadius, J. Nilsson, and M. Tenje, An acoustofluidic platform for non-contact trapping of cell-laden hydrogel droplets compatible with optical microscopy, *Biomicrofluidics* **13**, 044101 (2019).

- [36] B. Fan, F. Li, L. Chen, L. Shi, W. Yan, Y. Zhang, S. Li, X. Wang, X. Wang, and H. Chen, Photovoltaic Manipulation of Water Microdroplets on a Hydrophobic LiNbO_3 Substrate, *Phys. Rev. Appl.* **7**, 064010 (2017).
- [37] K. M. Mambetova, S. M. Shandarov, and A. I. Tatyannikov, Aggregation of dielectric nanoparticles on the x-cut of $\text{LiNbO}_3\text{:Cu}$ crystal by electric fields of photorefractive holograms, *Russ. Phys. J.* **62**, 658 (2019).
- [38] L. Arizmendi, Photonic applications of lithium niobate crystals, *Phys. Status Solidi (a)* **201**, 253 (2004).
- [39] I. Nee, M. Müller, K. Buse, and E. Krätzig, Role of iron in lithium-niobate crystals for the dark-storage time of holograms, *J. Appl. Phys.* **88**, 4282 (2000).
- [40] N. V. Kukhtarev, V. B. Markov, S. G. Odulov, M. S. Soskin, and V. L. Vinetskii, Holographic storage in electrooptic crystals. I. steady state, *Ferroelectrics* **22**, 949 (1978).
- [41] J. F. Muñoz-Martínez, J. B. Ramiro, A. Alcázar, A. García-Cabañes, and M. Carrascosa, Electrophoretic Versus Dielectrophoretic Nanoparticle Patterning Using Optoelectronic Tweezers, *Phys. Rev. Appl.* **7**, 064027 (2017).
- [42] J. F. Muñoz-Martínez, I. Elvira, M. Jubera, A. García-Cabañes, J. B. Ramiro, C. Arregui, and M. Carrascosa, Efficient photo-induced dielectrophoretic particle trapping on Fe:LiNbO_3 for arbitrary two dimensional patterning, *Opt. Mat. Express* **5**, 1137 (2015).
- [43] C. M. Phan, B. Allen, L. B. Peters, T. N. Le, and M. O. Tale, Can water float on oil?, *Langmuir* **28**, 4609 (2012).
- [44] C. M. Phan, Stability of a floating water droplet on an oil surface, *Langmuir* **30**, 768 (2014).
- [45] S. Grilli, L. Miccio, V. Vespini, A. Finizio, S. De Nicola, and Pietro Ferraro, Liquid micro-lens array activated by selective electrowetting on lithium niobate substrates, *Opt. Express* **16**, 8084 (2008).
- [46] See the Supplemental Material at <http://link.aps.org/supplemental/10.1103/PhysRevApplied.14.024046> for videos of the aqueous droplet manipulation processes shown in Figs. 3, 5, 6, and 7; a video of the simulation of the time evolution of the charge density; and photoinduced electric field vectors for the parallel configuration represented in Fig. 8(f).
- [47] F. Agulló-López, G. F. Calvo, and M. Carrascosa, *Fundamentals of Photorefractive Phenomena in Photorefractive Materials and Their Applications 1, Chapter 3* (Springer, New York, 2006).
- [48] C. Arregui, J. B. Ramiro, A. Alcázar, A. Méndez, H. Burgos, A. García-Cabañes, and M. Carrascosa, Optoelectronic tweezers under arbitrary illumination patterns: Theoretical simulations and comparison to experiment, *Opt. Express* **22**, 29099 (2014).
- [49] J. F. Muñoz-Martínez, A. Alcázar, and M. Carrascosa, Time evolution of photovoltaic fields generated by arbitrary light patterns in z-cut $\text{LiNbO}_3\text{:Fe}$: Application to optoelectronic nanoparticle manipulation, *Opt. Express* **28**, 18085 (2020).
- [50] A. Puerto, J. F. Muñoz-Martín, A. Mendez, L. Arizmendi, A. García-Cabañes, F. Agulló-López, and M. Carrascosa, Synergy between pyroelectric and photovoltaic effects for optoelectronic nanoparticle manipulation, *Opt. Express* **27**, 804 (2019).
- [51] L. Miccio, P. Memmolo, S. Grilli, and P. Ferraro, All-optical microfluidic chips for reconfigurable dielectrophoretic trapping through SLM light induced patterning, *Lab Chip* **12**, 4449 (2012).
- [52] P. Ferraro, S. Coppola, S. Grilli, M. Paturzo, and V. Vespini, Dispensing nano-pico droplets and liquid patterning by pyroelectrodynamics shooting, *Nat. Nanotechnol.* **5**, 429 (2010).
- [53] V. Vespini, S. Coppola, S. Grilli, M. Paturzo and P. Ferraro, Pyroelectric adaptive nanodispenser (PYRANA) micro-robot for liquid delivery on a target, *Lab Chip* **11**, 3148 (2011).
- [54] E. Muñoz-Cortés, A. Puerto, A. Blázquez-Castro, L. Arizmendi, J. L. Bella, C. López-Fernández, M. Carrascosa, and A. García-Cabañes, Optoelectronic generation of bioaqueous femto-droplets base on the bulk photovoltaic effect, *Opt. Lett.* **45**, 1164 (2020).